Bioconjugate Chemistry

Article

Cite This: *Bioconjugate Chem.* 2020, 31, 360−368

pubs.acs.org/bc

Multimodal Positron Emission Tomography Imaging to Quantify Uptake of ^{89}Zr-Labeled Liposomes in the Atherosclerotic Vessel Wall

Mark E. Lobatto,[†,‡,▼] Tina Binderup,[†,§,▼] Philip M. Robson,[†] Luuk F. P. Giesen,[†] Claudia Calcagno,[†] Julia Witjes,[†] Francois Fay,[†,○] Samantha Baxter,[†] Chang Ho Wessel,[†] Mootaz Eldib,[†] Jason Bini,[†] Sean D. Carlin,[∥] Erik S. G. Stroes,[⊥] Gert Storm,[#,¶] Andreas Kjaer,[§] Jason S. Lewis,[∥,●] Thomas Reiner,[∥,■] Zahi A. Fayad,[†] Willem J. M. Mulder,*[,†,△,▲] and Carlos Pérez-Medina*[,†,⬢]

[†]Translational and Molecular Imaging Institute, Icahn School of Medicine at Mount Sinai, New York, New York 10029, United States

[‡]Department of Radiology, Spaarne Gasthuis, 2035 RC Haarlem, The Netherlands

[§]Department of Clinical Physiology, Nuclear Medicine & PET and Cluster for Molecular Imaging, Rigshospitalet & University of Copenhagen, 2100 Copenhagen, Denmark

[∥]Department of Radiology, Memorial Sloan Kettering Cancer Center, New York, New York 10065, United States

[⊥]Department of Vascular Medicine, Academic Medical Center, 1105 AZ Amsterdam, The Netherlands

[#]Department of Targeted Therapeutics, MIRA Institute, University of Twente, 7522 NB Enschede, The Netherlands

[¶]Utrecht Institute for Pharmaceutical Sciences, Utrecht University, 3512 JE Utrecht, The Netherlands

[●]Program in Molecular Pharmacology, Memorial Sloan Kettering Cancer Center, New York, New York 10065, United States

[△]Laboratory of Chemical Biology, Department of Biomedical Engineering and Institute for Complex Molecular Systems, Eindhoven University of Technology, 5612 AZ Eindhoven, The Netherlands

[⬢]Centro Nacional de Investigaciones Cardiovasculares Carlos III, 28029 Madrid, Spain

[○]Institut Galien Paris Sud UMR 8612, Faculté de Pharmacie, CNRS, Univ. Paris-SudUniversité Paris-Saclay, 92290 Châtenay-Malabry, France

[■]Chemical Biology Program, Memorial Sloan Kettering Cancer Center, New York, New York 10065, United States

[▲]Department of Oncological Sciences, Icahn School of Medicine at Mount Sinai, New York, New York 10029, United States

Supporting Information

ABSTRACT: Nanotherapy has recently emerged as an experimental treatment option for atherosclerosis. To fulfill its promise, robust noninvasive imaging approaches for subject selection and treatment evaluation are warranted. To that end, we present here a positron emission tomography (PET)-based method for quantification of liposomal nanoparticle uptake in the atherosclerotic vessel wall. We evaluated a modular procedure to label liposomal nanoparticles with the radioisotope zirconium-89 (^{89}Zr). Their biodistribution and vessel wall targeting in a rabbit atherosclerosis model was evaluated up to 15 days after intravenous injection by PET/computed tomography (CT) and PET/magnetic resonance imaging (PET/MRI). Vascular permeability was assessed *in vivo* using three-dimensional dynamic contrast-enhanced MRI (3D DCE-MRI) and *ex vivo* using near-infrared fluorescence (NIRF) imaging. The ^{89}Zr-radiolabeled liposomes displayed a biodistribution pattern typical of long-circulating nanoparticles. Importantly, they markedly accumulated in atherosclerotic lesions in the abdominal aorta, as evident on PET/MRI and confirmed by autoradiography, and this uptake moderately correlated with vascular permeability. The method presented herein facilitates the development of nanotherapy for atherosclerotic disease as it provides a tool to screen for nanoparticle targeting in individual subjects' plaques.

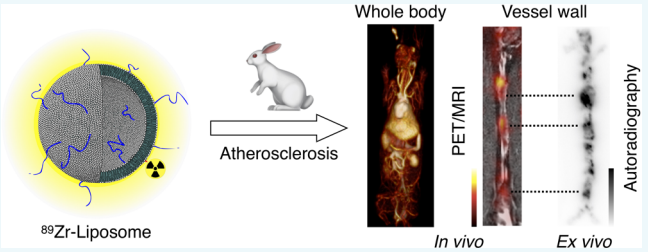

INTRODUCTION

Atherosclerosis, the leading cause of cardiovascular disease complications such as myocardial infarction and stroke, is a chronic inflammatory disease affecting the major arteries.[1] Its progression is driven by the infiltration of lipids and immune

Special Issue: Molecular Imaging

Received: April 9, 2019
Revised: May 10, 2019
Published: May 16, 2019

DOI: 10.1021/acs.bioconjchem.9b00256
Bioconjugate Chem. 2020, 31, 360−368

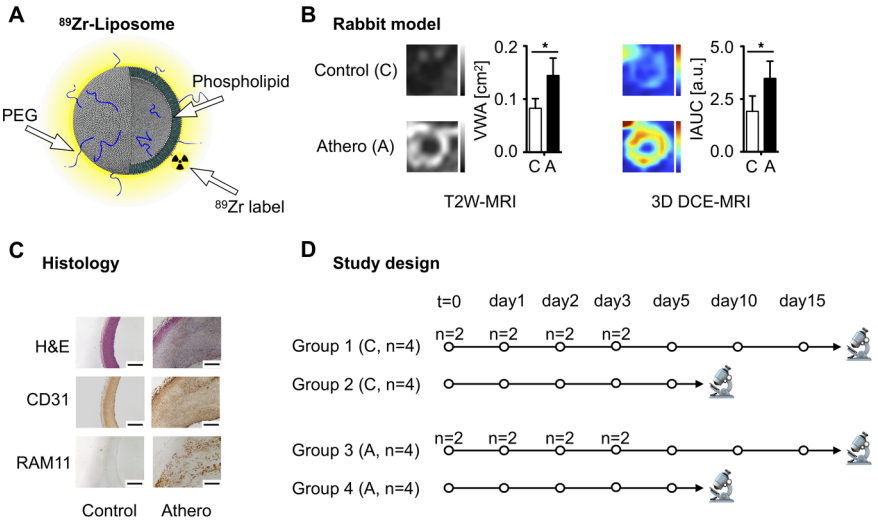

Figure 1. Formulation, animal model, and study design. (A) Modular labeling of zirconium-89 (^{89}Zr) liposomes. The outer layer with poly(ethylene glycol) (PEG) ensures long-circulating properties. (B) Vessel wall area (VWA) in atherosclerotic rabbits was significantly larger than in control animals (0.15 vs 0.08 cm^2; $P < 0.001$), as was vascular permeability measured by 3D dynamic contrast enhanced-magnetic resonance imaging (3D DCE-MRI) (3.48 vs 1.92 au; $P < 0.001$). (C) Representative aortic sections stained with hematoxylin and eosin (H&E), CD31 antibodies for endothelial cells, and RAM-11 antibodies for macrophages reveal a markedly thickened vessel wall in rabbits with atherosclerosis, with intraplaque neovessels and abundant macrophages compared to the normal vessel wall in control rabbits. Magnification 10×, scale bar 2 mm. (D) Study design showing the number of rabbits allotted to control and atherosclerotic groups, as well as when the animals were scanned and when they were euthanized. C = control, A = atherosclerotic.

cells into the vessel wall.[2] Nanomedicine has recently emerged as a potential therapeutic option for atherosclerosis,[3,4] with the first clinical trials recently conducted by our group.[5] Unlike cancer, atherosclerosis is a slowly progressing—initially mild—disease process, which complicates the implementation of nanotherapeutics, as the therapeutic window might be unclear. The integration of nanomedicine in atherosclerosis management can greatly benefit from companion imaging, allowing the identification of amenable subjects and providing feedback on atherosclerotic burden.[6] For example, imaging may assist the development of novel nanotherapies by noninvasively examining biodistribution, the extent of disease, and, finally, therapeutic outcomes.[4]

In previous studies, we have shown that intravenously injected long-circulating nanoparticles accumulate in atherosclerotic lesions in areas of enhanced permeability in animal models, as well as in atherosclerotic lesions in patients with cardiovascular disease.[5,7,8] Primarily, these nanotherapeutics were colocalized with macrophages, main contributors to atherosclerotic plaque inflammation, and concurrent destabilization. Hence, the inclusion of therapeutics into nanoparticles can facilitate local enrichment of anti-inflammatory compounds, potentially increasing efficacy and decreasing adverse effects.[9]

Radiolabeling of nanoparticles is a valuable approach to determine pharmacokinetics and biodistribution by *ex vivo* radioactivity quantification methods.[10] The sensitivity of the technique requires minimal modification to nanoparticles and therefore does not—or marginally at most—compromise their function.[11] More recently, PET or single-photon emission computed tomography (SPECT) imaging of radiolabeled nanoparticles has allowed the quantitative assessment of biodistribution *in vivo*, albeit a limitation of nuclear imaging is its low spatial resolution and dearth of anatomical information.[12,13] This is especially the case in the context of atherosclerosis, where small plaques can occur in multiple regions of the arterial tree, necessitating anatomical reference.

The latest advancement in clinical imaging techniques, i.e., PET/MRI in a single hybrid system, has the capability to greatly diversify acquired information. The addition of MRI allows the thorough characterization of atherosclerotic burden and the vessel wall in high resolution, a feature that is more difficult to achieve with CT due to its reduced ability to always distinguish plaque components.[14] New MRI protocols that, in addition to anatomical information, can concomitantly acquire functional information, such as the quantification of arterial wall microvascular permeability through dynamic contrast enhanced (DCE) imaging, can be of great value.[15] Moreover, by increasing the length of PET acquisition to match that of the MR scan, simultaneous PET/MRI allows a significant radiation dose reduction while preserving quantification and image quality.[16]

In this study, liposomes were labeled with ^{89}Zr, a positron emitter with a relatively long half-life (78.41 h) and a favorable positron range. Clinical PET/CT and PET/MRI systems were used to improve our understanding of the *in vivo* behavior of the nanoparticles, and the relation of their accumulation with plaque permeability, in a rabbit model of atherosclerosis.

RESULTS

Radiolabeling of Liposomal Nanoparticles with ^{89}Zr.

Long circulating liposomes, previously applied in experimental atherosclerosis and human studies,[5,7,17] were prepared by lipid-film hydration and subsequently labeled with ^{89}Zr in a modular fashion.[18] The polyethylene glycol (PEG) coating ensures long-circulating properties, due to initial avoidance of capture by the mononuclear phagocyte system (MPS), mainly the liver, spleen, and bone marrow, thereby avoiding rapid *in vivo* clearance.[19] A schematic representation of the nanoparticle is depicted in Figure 1A. The radiochemical yield was 72 ± 16% ($n = 6$) with a radiochemical purity of >99%. Radiolabeled liposomes had a mean effective diameter of 106.0 ± 5.2 nm and a dispersity index of 0.14 ± 0.01 ($n = 6$). Liposome composition and size exclusion

DOI: 10.1021/acs.bioconjchem.9b00256
Bioconjugate Chem. 2020, 31, 360−368

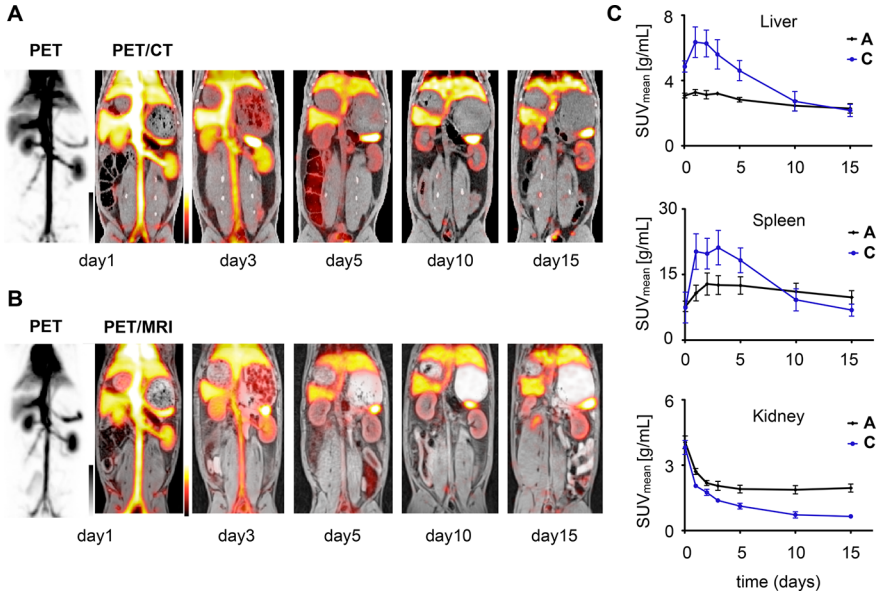

Figure 2. Liposome biodistribution in rabbits. (A, B) Biodistribution of liposomes is shown with representative coronal images in a control animal obtained by positron emission tomography (PET) and combined PET-computed tomography (PET/CT, A) or magnetic resonance imaging (PET/MRI, B), showing initial blood pool activity and activity in the mononuclear phagocyte system, such as the liver and spleen at later time points. (C) PET-derived time−activity curves in organs of atherosclerotic (A, black trace) and control (C, blue trace) rabbits. Differences in long-term biodistribution between the two groups can be seen, mainly attributed to the high-cholesterol diet inducing end organ damage in the liver.

chromatograms are shown in Supporting Information (SI) Figure 1.

MR Imaging-Based Characterization of the Rabbit Atherosclerosis Model. We performed MRI characterization of the vessel wall of New Zealand white rabbits that received double balloon injuries of the abdominal aorta and a high-cholesterol diet, a well-established animal model of atherosclerosis.[20] The animal model is of interest as it can be scanned on clinical systems and has heterogeneous atherosclerotic plaque formation along the abdominal aorta. First, T2-weighted MR images were acquired to characterize vessel wall morphology, in which rabbits subjected to the above protocol had a markedly thicker vessel wall than healthy control rabbits fed a regular chow-diet, where the vessel wall was barely discernible (0.145 vs 0.083 cm^2; $P < 0.001$: Figure 1B). Moreover, 3D DCE-MRI was performed, a technique that allows quantification of microvascular permeability of the arterial wall over an extensive vascular region by acquiring data prior to and continuously after the injection of Gd-DTPA, a clinical MRI contrast agent.[21] From this, data kinetics can be derived, which showed that the vessel wall of atherosclerotic rabbits was highly permeable compared to the vessel wall of healthy control animals, in line with what has been observed previously (3.48 vs 1.92 au; $P = 0.001$: Figure 1B).[21] Representative histological slides in Figure 1C reveal a normal vessel wall without macrophages and neovasculature, in contrast to the prominently thickened vessel wall in atherosclerotic rabbits with intraplaque neovessels (CD31 staining) as well as macrophage accumulation (RAM-11 staining).

Imaging Biodistribution with PET/CT and PET/MRI. Animals received a single intravenous injection of ^{89}Zr-liposomes, after which they were subjected to serial *in vivo* PET/CT and PET/MRI sessions on clinical scanners. The study design displayed in Figure 1D indicates the time points healthy control and atherosclerotic animals were subjected to imaging. The biodistribution of ^{89}Zr-liposomes in healthy control rabbits was evaluated by imaging with both PET/CT and PET/MRI at 5 different time points (Figure 1D). Representative coronal images of the abdomen of the rabbits in a maximum intensity projection (MIP) of PET as well as on fused PET/CT images are shown in Figure 2A, where activity on day 1 mainly derives from the blood pool and highly vascularized organs, such as the kidneys and liver. Over time, activity in the blood pool decreased until the liposomes' complete vascular clearance, with eventual predominant activity in MPS organs, mainly the liver and spleen up to day 15.

Analogous to PET/CT, PET/MRI showed an expected comparable distribution pattern (Figure 2B). Liver, spleen, and kidneys were traced to quantify biodistribution as standardized uptake values (SUV), using the mean SUV (SUV_{mean}, Figure 2C). Values were subsequently compared to atherosclerotic rabbits. Uptake in liver and spleen was markedly higher in control compared to atherosclerotic rabbits up until day 5 (4.6 vs 2.8 g/mL for liver, and 18.3 vs 12.5 g/mL for spleen) after which the uptake was at similar levels for both liver and spleen. This difference is likely due to impaired liver function in atherosclerotic rabbits caused by steatohepatitis, fattening of the liver, triggered by the high-cholesterol diet. Quantitative data shown in the graphs (Figure 2C) corroborate the visible uptake in the organs shown in Figure 2A and B. Importantly, PET/CT and PET/MRI data show a high degree of correlation in both atherosclerotic and healthy control rabbits ($\rho = 0.98$ and 0.86, respectively; $P < 0.001$). A similar high correlation was found between gamma counting and PET/CT as well as PET/MRI in both atherosclerotic and healthy control animals (SI Figure 2).

Visualizing Nanoparticle Targeting of the Vessel Wall by PET/CT and PET/MRI. After systematic interrogation of biodistribution, we investigated nanoparticle vessel wall accumulation in atherosclerotic rabbits by both PET/CT and PET/MRI. Representative coronal images of both modalities at different time points are shown in Figure 3A,B, as well as a 3D reconstruction of PET activity in Figure 3C at day 0. Additional

DOI: 10.1021/acs.bioconjchem.9b00256
Bioconjugate Chem. 2020, 31, 360−368

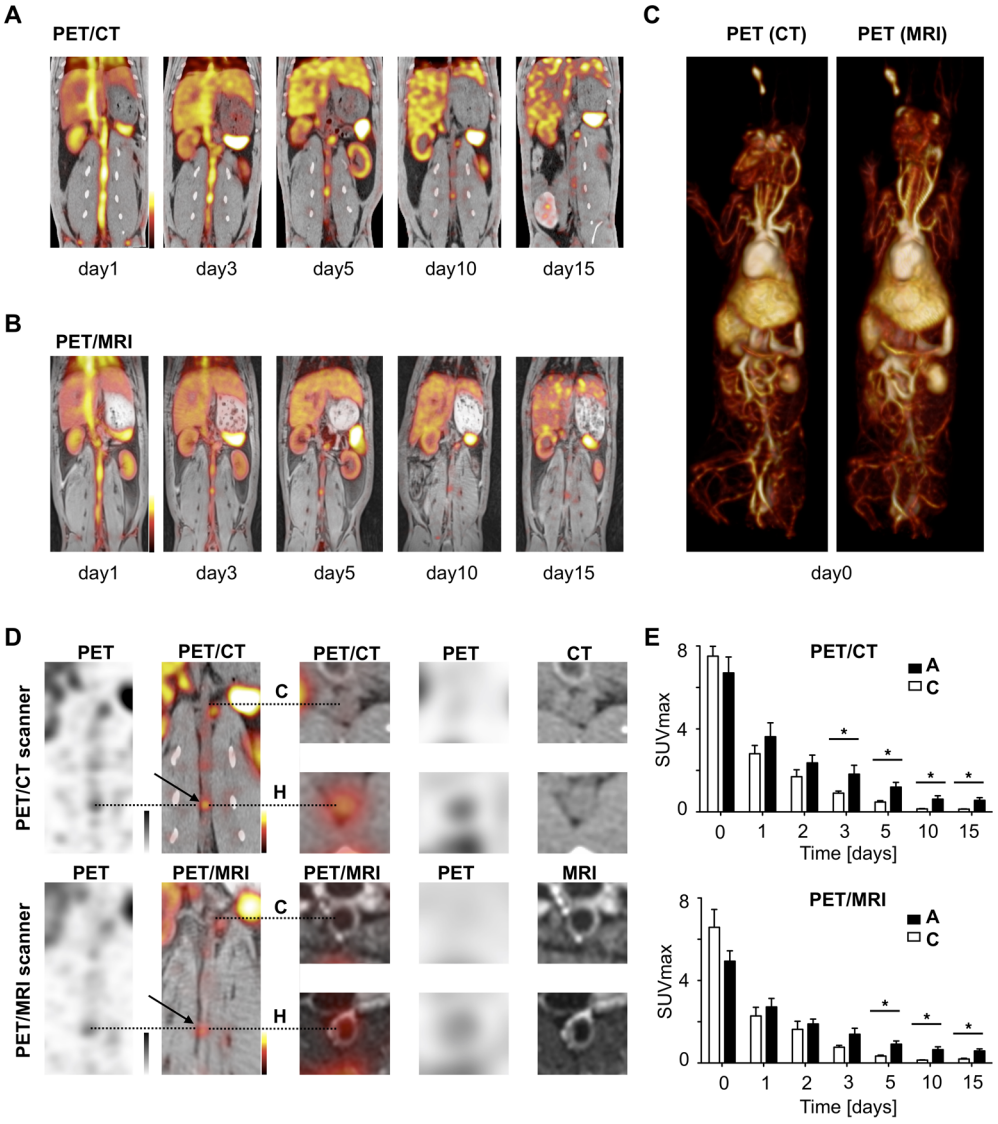

Figure 3. Vessel wall targeting in rabbits with atherosclerosis. (A, B) Biodistribution in atherosclerotic rabbits. Representative coronal PET/CT (A) and PET/MR (B) images reveal patchy uptake in the abdominal aorta, which is better appreciated at later time points after clearance of liposomes from the blood pool. (C) PET maximum intensity projections (MIP) from the same rabbit, obtained with PET/CT and PET/MRI scanners on day 0 (1 h post injection). (D) PET/CT (top) and PET/MRI (bottom) images taken at PET cold (C) and hot spot (H, indicated by arrows) sections for the same animal 10 days post injection. Co-localization of radioactivity to thickened vessel wall sections is revealed by PET/MRI. (E) Radioactivity concentration in the vessel wall, expressed as average of maximum standardized uptake values (SUV_{max}) from the entire abdominal aorta in atherosclerotic and control rabbits show significantly higher accumulation at 3 days and onward. Both PET/CT and PET/MRI exhibit similar values. C = control animals, A = atherosclerotic animals.

3D volume-rendered images are shown in SI Figure 3 and Movies 1 and 2. Interestingly, after blood radioactivity clearance at 3 days post administration, distinct hot spots could be observed at different segments along the abdominal aorta in atherosclerotic animals. This patchy activity distribution was in contrast with only background activity in control rabbits. Axial PET/CT images of atherosclerotic rabbits do not allow the anatomical localization of hot spots within the vessel wall. In contrast, PET/MRI, with superb soft tissue contrast and vessel wall delineation on T2-weighted MR images, allows hot spot colocalization within the thickened vessel wall (Figure 3D). Interestingly, in focal areas without ^{89}Zr uptake, the vessel wall was also thickened. In Figure 3E, quantification of maximum SUV (SUV_{max}) of the entire vessel wall of the abdominal aorta in atherosclerotic rabbits reveals high uptake of ^{89}Zr-liposomes in the vessel wall compared to negligible uptake in the control animals. After clearance from blood, the uptake becomes significantly higher in atherosclerotic compared to control rabbits from day 3 (1.8 vs 0.9 g/mL) and onward.

Pharmacokinetics and *ex Vivo* Quantification. Pharmacokinetic data were derived from blood drawn at different time points, demonstrating a long half-life of 19 h for control rabbits (Figure 4A), which is comparable to prior results in the same model.[22] In atherosclerotic rabbits, the circulation half-life was longer (29 h), probably due to the aforementioned liver damage. After sacrifice, organs were weighed and radioactivity accumulation was evaluated in a gamma counter confirming the *in vivo* measurements with expectedly high uptake in tissues of the MPS (liver, spleen, and bone marrow), which remained high throughout 15 days of observation (Figure 4B).

Thirty minutes prior to sacrifice, Evans Blue was injected, a dye that can be visualized by fluorescence imaging and

DOI: 10.1021/acs.bioconjchem.9b00256
Bioconjugate Chem. 2020, 31, 360−368

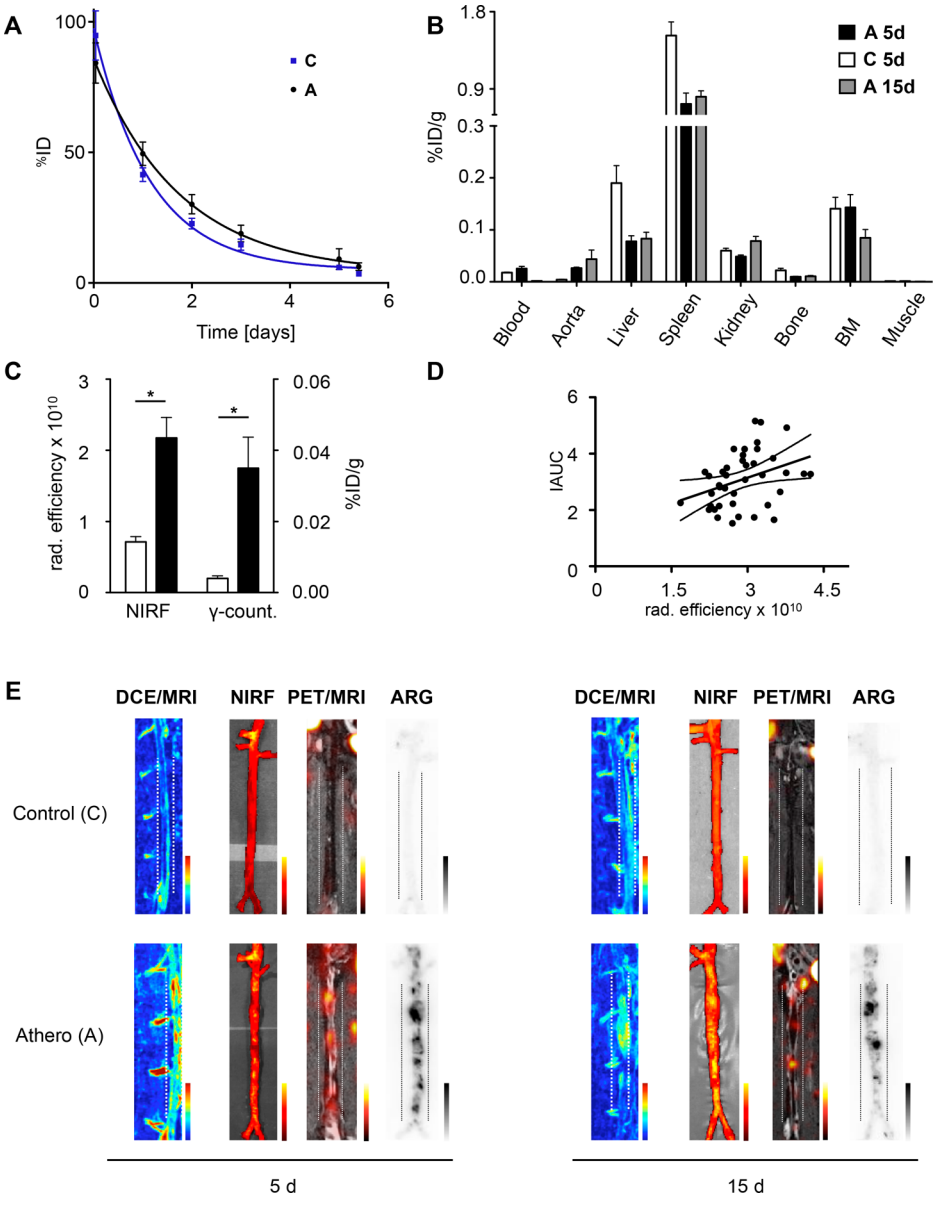

Figure 4. *Ex vivo* quantification of liposomal uptake. (A) Pharmacokinetics of ^{89}Zr-liposomes. Blood circulation half-life in control rabbits was 19 h, versus 29 h in atherosclerotic rabbits. (B) *Ex vivo* gamma counting quantification of organ distribution reveals high activity concentration in the MPS, predominantly liver and spleen. (C) Quantification of Evans Blue in abdominal aortas as a marker of permeability measured by near-infrared fluorescence (NIRF) imaging revealed a significantly higher signal in atherosclerotic rabbits versus control rabbits (2.2×10^{10} vs 0.7×10^{10} μW/cm^2; $P < 0.001$). A significantly higher accumulation of ^{89}Zr in the abdominal aortas measured by gamma-counter (0.026 vs 0.004% injected dose per gram; $P < 0.001$) was found as well. (D) Correlation between *in vivo* and *ex vivo* measured vascular permeability, as determined by 3D DCE-MRI and NIRF imaging, respectively ($\rho = 0.35$; $P = 0.03$). IAUC: intensity area-under-the-curve. (E) *In vivo* and *ex vivo* measurement of vascular permeability by 3D DCE/MRI and NIRF imaging, respectively, reveals low permeability in control animals at 5 and 15 days with focal regions of increased permeability in atherosclerotic rabbits. Similar to PET/MR imaging, *ex vivo* autoradiography (ARG) revealed a patchy pattern of radioactivity deposition in atherosclerotic aortas, while no focal accumulation was seen in control rabbits. Dashed lines delineate the abdominal aortas in the images as a reference guide. BM = bone marrow.

extravasates at regions of vascular permeability for macromolecules.[8,23] In line with the significantly higher concentration of ^{89}Zr in the abdominal aorta of atherosclerotic rabbits measured with the gamma-counter (0.004 vs 0.026% injected dose per gram; $P < 0.001$), near-infrared fluorescence (NIRF) imaging confirmed significantly higher vascular permeability in atherosclerotic vs control rabbits (2.2×10^{10} vs 0.7×10^{10} μW/cm^2; $P < 0.001$) (Figure 4C). *Ex vivo* imaging of the aortas by NIRF was compared with 3D DCE-MRI, showing a similar positive correlation between the 2 readouts of vascular permeability ($\rho = 0.35$; $P = 0.03$) (Figure 4D) as previously reported.[21] Taken together, all imaging techniques—3D DCE-MRI, PET/MRI, NIRF, and autoradiography—show similar regions of uptake in atherosclerotic rabbits, compared to no uptake in healthy controls (Figure 4E). Importantly, liposomes tended to accumulate in thicker, more permeable aortic regions, as attested by the significant correlation between ^{89}Zr PET SUV_{max} and both MRI-based vessel wall area and permeability measurements (SI Figure 4).

DOI: 10.1021/acs.bioconjchem.9b00256
Bioconjugate Chem. 2020, 31, 360−368

DISCUSSION

In this study, we have shown that ^{89}Zr-labeled liposomes accumulate in the vessel wall of rabbits with atherosclerosis, which we demonstrated noninvasively using a multimodal imaging approach. To the best of our knowledge, this is the first example of multimodal PET/MRI and PET/CT on clinical scanners that shows the accumulation of long-circulating nanoparticles in the vessel wall. In the context of atherosclerosis, the vast majority of nanoparticulate agents reported are used for diagnostic imaging purposes. For instance, a small biodegradable 5 nm ^{18}F-labeled dextran nanoparticle with renal clearance was used to noninvasively visualize atherosclerotic plaques and infarcted myocardial tissue due to their high affinity for lesional macrophages.[24] In another study, multimodal nanoparticles that were developed with both MRI and PET contrast agents have also been used for PET and MRI to monitor macrophage accumulation in atherosclerotic lesions using preclinical imaging modalities.[25] More recently, we reported a method to visualize the *in vivo* behavior of high-density lipoproteins by multimodal PET imaging.[26]

Establishing reliable quantitative determination methods of nanoparticle distribution in the body following systemic administration remains one of the main challenges facing nanomedicine.[27] Of the many techniques available, radioactivity-based methods are uniquely suited due to their high sensitivity. Moreover, the use of positron emitters allows noninvasive visualization of biodistribution by PET imaging. However, some concerns may be related to the behavior of the radiolabeled material compared with the unlabeled fraction. In a previous study using a fluorescently labeled analog of the ^{89}Zr-liposomes, we demonstrated the robustness of the nanoplatform.[18] Furthermore, in a separate study we found that ^{89}Zr-liposomes showed nearly identical tumor targeting features to commercial liposomal doxorubicin,[28] which has very similar chemical composition, size, and surface charge, indicating that this radiolabeling strategy does not affect their *in vivo* behavior. The use of ^{89}Zr (physical half-life = 78.4 h) is mandated for monitoring long-circulating materials, especially if the target is the vessel wall, to allow for blood pool signal clearance. Thus, we were able to clearly visualize radioactivity accumulation in the aorta from atherosclerotic animals and noninvasively measure this uptake only after 3 days post administration. Moreover, thanks to ^{89}Zr's above-mentioned long half-life, we were able to noninvasively monitor the nanoparticles' fate for a period of up to 15 days post injection. While using ^{89}Zr could pose dosimetry concerns due to its long half-life, its slow physical decay allows administration of lower doses. Indeed, long-lived PET isotopes like ^{89}Zr and ^{124}I have been used to radiolabel monoclonal antibodies for so-called immuno-PET applications in clinical studies with patients receiving doses as low as 37 MBq.[29] Moreover, the expected sensitivity improvements of future PET scanners will allow further reduction in the injected radioactivity without compromising image quality.[30]

In this study, we found a moderate correlation between vessel wall DCE-MRI-derived permeability measurements and PET-based ^{89}Zr-liposome uptake. However, due to high blood pool signal, the latter could only be measured reliably at 3 days post administration and onward. This is in line with our previous work, where we found that liposomal accumulation in the atherosclerotic vessel wall initially correlates strongly with *in vivo* and *ex vivo* measures of vascular permeability, similar to tumor enhanced permeability and retention phenomena. Over time, however, the correlation wanes as the nanoparticles disperse throughout the plaque.[7]

New methods to easily quantify biodistribution and characterize atherosclerotic burden and subsequent uptake of nanoparticles in the vessel wall noninvasively can be of great value for the development of nanotherapeutics. The sensitivity of PET together with the exceptional soft-tissue contrast of MRI provided vastly detailed anatomical and functional imaging. We have previously shown that liposomal nanoparticles loaded with glucocorticoids dampened inflammation effectively in a rabbit model of atherosclerosis.[17] Unfortunately, further development in a first-in-human small scale clinical trial showed no clinical effect in first instance, although an exact cause could not be identified.[5] In such studies in small patient populations, with a very heterogeneous disease process, it is of paramount importance to implement screening procedures to identify those subjects that would most likely benefit from therapy.[31] Using the same ^{89}Zr-labeled nanoparticle described in this study as a "nanoreporter", we were able to predict the efficacy of an anticancer nanotherapy based on the information obtained from a single imaging session.[28] Similarly, with the tools to monitor targeting, atherosclerotic burden, and biodistribution presented here, patient selection for anti-atherosclerosis nanotherapy can potentially be optimized. With the advent of the precision medicine era, this type of screening procedure should be at the forefront to provide personalized care based on individual phenotypical traits.

In conclusion, we have developed a tool to quantify nanoparticle uptake in the atherosclerotic vessel wall, image biodistribution, and assess atherosclerotic burden in a single noninvasive multimodal imaging session with PET/MRI.

EXPERIMENTAL PROCEDURES

Materials. Phospholipids 1,2-dipalmitoyl-*sn*-glycero-3-phosphocholine (DPPC), 1,2-distearoyl-*sn*-glycero-3-phosphoethanolamine-*N*-[amino(polyethylene glycol)-2000] (DSPE-PEG2000), 1,2-distearoyl-*sn*-glycero-3-phosphoethanolamine (DSPE), and cholesterol were purchased from Avanti Polar Lipids (Alabaster, AL). 1-(4-Isothiocyanatophenyl)-3-[6,17-dihyroxy-7,10,18,21-tetraoxo-27-[*N*-acetylhy-droxylamino)-6,11,17,22-tetraazaheptaeicosane]thiourea (DFO-*p*-NCS) was acquired from Macrocyclics (Plano, TX). The phospholipid-chelator 1,2-distearoyl-*sn*-glycero-3-phosphoethanolamine-deferoxamine B (DSPE-DFO, SI Figure 1B) was synthesized as previously described.[18] All other chemicals were purchased from Sigma-Aldrich (St. Louis, MO) and were used without further modification. ^{89}Zr was produced at Memorial Sloan-Kettering Cancer Center on an EBCO TR19/9 variable-beam energy cyclotron (Ebco Industries Inc., British Columbia, Canada) via the ^{89}Y(p,n)^{89}Zr reaction.

Preparation of ^{89}Zr-Labeled Liposomes. Ready-to-label liposomes were prepared using a sonication method as previously described.[18] Briefly, a lipid film composed of DPPC, cholesterol, DSPE-PEG2000, and DSPE-DFO was produced by evaporation of a chloroform solution. The film was hydrated with phosphate buffered saline (PBS) and the resulting suspension sonicated for 25 min. For radiolabeling, a solution of deferoxamine B (DFO)-bearing liposomes in PBS was reacted with ^{89}Zr-oxalate at 40 °C for 2 h.[18] The labeled liposomes were purified by spin filtration using 100 kDa molecular weight cutoff tubes (Millipore, Billerica, MA). The concentrate was washed with sterile PBS and finally diluted with sterile PBS to the desired volume.

DOI: 10.1021/acs.bioconjchem.9b00256
Bioconjugate Chem. 2020, 31, 360−368

Animal Model Preparation. Eight New Zealand male white rabbits were fed a high-cholesterol diet and received two balloon angioplasties of the abdominal aortas to induce atherosclerotic lesions according to a well-established method.[20] Eight New Zealand male white rabbits fed a normal chow diet were used as healthy control animals. All intravenous injections were administered through 22-gauge catheters positioned in the marginal ear vein. Imaging was performed under anesthesia with a combination of Ketamine (35 mg/kg) and Xylazine (5 mg/kg), and Isofluorane was used as maintenance anesthesia.

All animal experiments were approved by the Institutional Animal Care and Use Committee at the Icahn School of Medicine at Mount Sinai.

Imaging Acquisition. After intravenous coinjection of 27.1 ± 3.6 MBq (mean ± SD) ^{89}Zr-liposomes and plain, non-radioactive liposomes in 5 mL PBS solution (at a combined dose of 50 μmol total lipid/kg body weight), rabbits were positioned in either a Siemens mCT Biograph PET/CT or a Siemens mMR 3T PET/MRI scanner in a body matrix coil. PET was acquired in 3D mode, 10 min for PET/MR and 7 min for PET/CT.

The parameters for PET/CT were set at: 140 kVp voltage; 43 mA tube current; 1000 ms exposure time; 1 mm slice thickness. Image reconstruction was performed with the algorithms point-spread function and time-of-flight (TOF). For PET/MRI, the scan was started after scout scans and were acquired along a radial VIBE MR sequence with the following parameters: 20 ms TR, 1.89 ms TE, 10° flip angle, and 1.1 mm^3 slice thickness. PET image attenuation correction was performed with a built-in MR based attenuation correction (MR-AC) map and image reconstruction using OP-OSEM algorithm.

A time-of-flight angiography was acquired to seek anatomical landmarks (renal arteries and iliac bifurcation). T2-weighted 3D anatomical MRI was performed using the Sampling Perfection with Application optimized Contrasts using different flip angle Evolution (SPACE) sequence, in the sagittal plane, starting from the left renal artery to the iliac bifurcation, with isotropic voxels of 0.6 × 0.6 × 0.6 mm^3. Other relevant imaging parameters were as follows: repetition time (TR), 1600 ms; echo time (TE), 118 ms; number of slices, 56; number of signal averages, 2; echo train length (ETL), 83.

Delayed enhancement and 3D DCE-MRI were acquired using a segmented fast low angle shot (FLASH) sequence, in the sagittal plane, also starting from the left renal artery to the iliac bifurcation, with isotropic voxels of 0.6 × 0.6 × 0.6 mm^3. Relevant imaging parameters were as follows: TR, 12.1 ms; TE, 5.7 ms; number of slices, 20; flip angle, 25°. For delayed enhancement, 8 signal averages were acquired, while for DCE-MRI only 1 signal average per time frame was acquired. The duration of each time frame for DCE-MRI was approximately 30 s, for a total of 18 dynamic frames acquired. After acquisition of 3 images, 0.1 mmol/kg of gadolinium (Gd) DTPA (diethylene-triaminepentacetate) (Magnevist, Bayer Schering Pharma) was injected at the rate of 0.5 mL/s, and flushed with 15 mL of saline solution at the same rate.

***Ex Vivo* Methods.** To perform the pharmacokinetic analysis, blood was withdrawn from the marginal ear vein at 30 min, and 24, 48, 72, and 120 h post injection of liposomes. Next, samples were weighed and radioactivity concentration was measured on a Wizard^2 2480 automatic gamma counter (PerkinElmer, Waltham, MA). For assessment of percent injected dose (% ID), blood volume was estimated using the formula (0.6 × bodyweight + 0.77) as previously described.[32] Following the final *in vivo* imaging session and 30 min prior to sacrifice animals were injected with 0.5% of 5 mL of Evans Blue (Sigma-Aldrich, St. Louis, MO) in PBS. Afterward rabbits were sacrificed using an overdose of pentobarbital and saline perfused. Next, pieces of organs were harvested, weighed, and counted using a Wizard^2 2480 automatic gamma counter for assessment of ^{89}Zr-liposome biodistribution.

Near-Infrared Fluorescence Imaging. Directly post sacrifice, the abdominal aortas were positioned on thick black paper and fluorescence images were acquired with an IVIS Spectrum Preclinical Imaging System (PerkinElmer, Waltham, MA). Excitation and emission wavelengths were set at 605 and 680 nm, respectively. The data were then measured as total radiant efficiency (μW/cm^2). Ten ROIs were placed from the left renal artery to the iliac bifurcation.

Autoradiography. Tissue samples were placed in a film cassette against a phosphorimaging plate to perform digital autoradiography (BASMS-2325, Fujifilm, Valhalla, NY) for 48 h at −20 °C. The phosphorimaging plates were set at a pixel resolution of 25 μm with a Typhoon 7000IP plate reader (GE Healthcare, Pittsburgh, PA).

Histology. A selection of healthy and atherosclerotic aortas was cut into 5-mm-thick sections and placed in 4% paraformaldehyde. A day later sections were paraffin embedded and cut into sections of 5 μm thickness and placed on slides. Slides were subsequently stained with hematoxylin and eosin, RAM-11 and CD-31 antibodies according to standard immunohistochemistry techniques.

Imaging Data Analysis. Osirix 7.0 MD was used for image analysis, by tracing regions of interest (ROI) on liver, kidneys, spleen, and abdominal aortas on fused PET and radial VIBE MRI images to quantify biodistribution. From these ROIs, SUVmax was derived. Plaque burden was analyzed by drawing ROIs on the abdominal aortas on T2 weighted images; from here, the vessel wall area was calculated. 3D DCE-MRI was analyzed by drawing ROIs on the delayed enhancement scan and superimposing these on the dynamic scan. IAUC maps were analyzed in MatLab using a custom-made program. For T2W scans, assessment of vessel wall thickness was calculated as outer vessel wall area minus inner vessel wall area.

Statistical Analysis. Data are presented as mean ± standard error of the mean. GraphPad Prism version 5.0 was used for data analysis. For comparison of group differences, unpaired Student's *t*-test was used when data followed a Gaussian distribution (analyzed by the D'Agostino-Pearson omnibus normality test). Otherwise, the Mann−Whitney U test was used. Pearson's *r* coefficients were calculated to determine correlation. *P* values <0.05 were deemed as significant.

■ ASSOCIATED CONTENT

Supporting Information

The Supporting Information is available free of charge on the ACS Publications website at DOI: 10.1021/acs.bioconjchem.9b00256.

Composition and size exclusion chromatogram of ^{89}Zr-labeled liposomes; Correlation between plaque radioactivity concentration values obtained *in vivo* and *ex vivo*; 3D volume-rendered whole-body PET images; Slice-by-slice correlation between SUV$_{max}$ and vessel wall area and permeability (PDF)

3D volume-rendered image (MOV)

3D volume-rendered image (MOV)

DOI: 10.1021/acs.bioconjchem.9b00256
Bioconjugate Chem. 2020, 31, 360−368

AUTHOR INFORMATION

Corresponding Authors

*E-mail: willem.mulder@mssm.edu.
*E-mail: carlos.perez-medina@mountsinai.org.

ORCID

Francois Fay: 0000-0001-7405-5600
Jason S. Lewis: 0000-0001-7065-4534
Thomas Reiner: 0000-0002-7819-5480
Willem J. M. Mulder: 0000-0001-8665-3878
Carlos Pérez-Medina: 0000-0002-6011-0629

Author Contributions

▼M.E.L. and T.B. have shared first authorship.

Notes

The authors declare no competing financial interest.

ACKNOWLEDGMENTS

This work was supported by the National Heart, Lung, and Blood Institute, National Institutes of Health, as a Program of Excellence in Nanotechnology (PEN) Award, Contract #HHSN268201000045C (Z.A.F.), NIH/NHLBI R01 HL071021 (Z.A.F.), R01 HL118440 (W.J.M.M.), R01 HL125703 (W.J.M.M.), NIH/NIBIB R01 EB009638 (Z.A.F), NWO Vidi 91713324 (W.J.M.M.), FP7 NANOATHERO and the Dutch network for Nanotechnology NanoNextNL in the subprogram "Drug Delivery". M.E.L was partially supported by the International Atherosclerosis Society and the foundation "De Drie Lichten" in The Netherlands. T.B. was supported by the Danish Council for Independent Research (DFF – 1333–00235A), The Danish Cancer Society (R71-A4285) and Rigshospitalets Research Foundation. We appreciate the funding support from the NIH MSKCC Center Grant (P30-CA08748).

REFERENCES

(1) Libby, P., Ridker, P. M., and Hansson, G. K. (2011) Progress and Challenges in Translating the Biology of Atherosclerosis. *Nature 473* (7347), 317–325.

(2) Falk, E. (2006) Pathogenesis of Atherosclerosis. *J. Am. Coll. Cardiol. 47*, C7–12.

(3) Tabas, I., and Glass, C. K. (2013) Anti-Inflammatory Therapy in Chronic Disease: Challenges and Opportunities. *Science 339* (6116), 166–172.

(4) Lobatto, M. E., Fuster, V., Fayad, Z. A., and Mulder, W. J. M. (2011) Perspectives and Opportunities for Nanomedicine in the Management of Atherosclerosis. *Nat. Rev. Drug Discovery 10* (11), 835–852.

(5) van der Valk, F. M., van Wijk, D. F., Lobatto, M. E., Verberne, H. J., Storm, G., Willems, M. C. M., Legemate, D. A., Nederveen, A. J., Calcagno, C., Mani, V., et al. (2015) Prednisolone-Containing Liposomes Accumulate in Human Atherosclerotic Macrophages upon Intravenous Administration. *Nanomedicine 11* (5), 1039–1046.

(6) Mulder, W. J. M., Jaffer, F. A., Fayad, Z. A., and Nahrendorf, M. (2014) Imaging and Nanomedicine in Inflammatory Atherosclerosis. *Sci. Transl. Med. 6*, 239sr1.

(7) Lobatto, M. E., Calcagno, C., Millon, A., Senders, M. L., Fay, F., Robson, P. M., Ramachandran, S., Binderup, T., Paridaans, M. P. M., Sensarn, S., et al. (2015) Atherosclerotic Plaque Targeting Mechanism of Long-Circulating Nanoparticles Established by Multimodal Imaging. *ACS Nano 9* (2), 1837–1847.

(8) Kim, Y., Lobatto, M. E., Kawahara, T., Lee Chung, B., Mieszawska, A. J., Sanchez-Gaytan, B. L., Fay, F., Senders, M. L., Calcagno, C., Becraft, J., et al. (2014) Probing Nanoparticle Translocation across the Permeable Endothelium in Experimental Atherosclerosis. *Proc. Natl. Acad. Sci. U. S. A. 111* (3), 1078–1083.

(9) Metselaar, J. M., and Storm, G. (2005) Liposomes in the Treatment of Inflammatory Disorders. *Expert Opin. Drug Delivery 2* (3), 465–476.

(10) Wunder, A., Thiele, A., Koslowski, M., Gantner, F., and Niessen, H. (2014) Nuclear Imaging to Support Anti-Inflammatory Drug Discovery and Development. *Q. J. Nucl. Med. Mol. Imaging Off. Publ. Ital. Assoc. Nucl. Med. [and] Int. Assoc. Radiopharmacol. (IAR), [and] Sect. Soc. Radiopharm. 58* (3), 290–298.

(11) Liu, Y., and Welch, M. J. (2012) Nanoparticles Labeled with Positron Emitting Nuclides: Advantages, Methods, and Applications. *Bioconjugate Chem. 23* (4), 671–682.

(12) Harrington, K. J., Mohammadtaghi, S., Uster, P. S., Glass, D., Peters, A. M., Vile, R. G., and Stewart, J. S. (2001) Effective Targeting of Solid Tumors in Patients with Locally Advanced Cancers by Radiolabeled Pegylated Liposomes. *Clin. Cancer Res. 7* (2), 243–254.

(13) Welch, M. J., Hawker, C. J., and Wooley, K. L. (2009) The Advantages of Nanoparticles for PET. *J. Nucl. Med. 50* (11), 1743–1746.

(14) Sanz, J., and Fayad, Z. A. (2008) Imaging of Atherosclerotic Cardiovascular Disease. *Nature 451* (7181), 953–957.

(15) Calcagno, C., Mani, V., Ramachandran, S., and Fayad, Z. A. (2010) Dynamic Contrast Enhanced (DCE) Magnetic Resonance Imaging (MRI) of Atherosclerotic Plaque Angiogenesis. *Angiogenesis 13* (2), 87–99.

(16) Eldib, M., Bini, J., Lairez, O., Faul, D. D., Oesingmann, N., Fayad, Z. A., and Mani, V. (2015) Feasibility of (18)F-Fluorodeoxyglucose Radiotracer Dose Reduction in Simultaneous Carotid PET/MR Imaging. *Am. J. Nucl. Med. Mol. Imaging 5* (4), 401–407.

(17) Lobatto, M. E., Fayad, Z. A., Silvera, S., Vucic, E., Calcagno, C., Mani, V., Dickson, S. D., Nicolay, K., Banciu, M., Schiffelers, R. M., et al. (2010) Multimodal Clinical Imaging to Longitudinally Assess a Nanomedical Anti-Inflammatory Treatment in Experimental Atherosclerosis. *Mol. Pharmaceutics 7* (6), 2020–2029.

(18) Pérez-Medina, C., Abdel-Atti, D., Zhang, Y., Longo, V. A., Irwin, C. P., Binderup, T., Ruiz-Cabello, J., Fayad, Z. A., Lewis, J. S., Mulder, W. J. M, et al. (2014) A Modular Labeling Strategy for In Vivo PET and Near-Infrared Fluorescence Imaging of Nanoparticle Tumor Targeting. *J. Nucl. Med. 55* (10), 1706–1712.

(19) Klibanov, A. L., Maruyama, K., Torchilin, V. P., and Huang, L. (1990) Amphipathic Polyethyleneglycols Effectively Prolong the Circulation Time of Liposomes. *FEBS Lett. 268* (1), 235–237.

(20) Lobatto, M. E., Calcagno, C., Metselaar, J. M., Storm, G., Stroes, E. S. G., Fayad, Z. A., and Mulder, W. J. M. (2012) Imaging the Efficacy of Anti-Inflammatory Liposomes in a Rabbit Model of Atherosclerosis by Non-Invasive Imaging. *Methods Enzymol. 508*, 211–228.

(21) Calcagno, C., Lobatto, M. E., Dyvorne, H., Robson, P. M., Millon, A., Senders, M. L., Lairez, O., Ramachandran, S., Coolen, B. F., Black, A., et al. (2015) Three-Dimensional Dynamic Contrast-Enhanced MRI for the Accurate, Extensive Quantification of Microvascular Permeability in Atherosclerotic Plaques. *NMR Biomed. 28* (10), 1304–1314.

(22) Lobatto, M. E., Calcagno, C., Otten, M. J., Millon, A., Ramachandran, S., Paridaans, M. P. M., van der Valk, F. M., Storm, G., Stroes, E. S. G., Fayad, Z. A., et al. (2015) Pharmaceutical Development and Preclinical Evaluation of a GMP-Grade Anti-Inflammatory Nanotherapy. *Nanomedicine 11* (5), 1133–1140.

(23) Lundeberg, E., Van Der Does, A. M., Kenne, E., Soehnlein, O., and Lindbom, L. (2015) Assessing Large-Vessel Endothelial Permeability Using near-Infrared Fluorescence Imaging–Brief Report. *Arterioscler., Thromb., Vasc. Biol. 35* (4), 783–786.

(24) Keliher, E. J., Ye, Y.-X., Wojtkiewicz, G. R., Aguirre, A. D., Tricot, B., Senders, M. L., Groenen, H., Fay, F., Perez-Medina, C., Calcagno, C., et al. (2017) Polyglucose Nanoparticles with Renal Elimination and Macrophage Avidity Facilitate PET Imaging in Ischaemic Heart Disease. *Nat. Commun. 8*, 8.

(25) Jarrett, B. R., Correa, C., Ma, K. L., and Louie, A. Y. (2010) In Vivo Mapping of Vascular Inflammation Using Multimodal Imaging. *PLoS One 5* (10), 1.

(26) Pérez-Medina, C., Binderup, T., Lobatto, M. E., Tang, J., Calcagno, C., Giesen, L., Wessel, C. H., Witjes, J., Ishino, S., Baxter, S.,

DOI: 10.1021/acs.bioconjchem.9b00256
Bioconjugate Chem. 2020, 31, 360–368

et al. (2016) In Vivo PET Imaging of HDL in Multiple Atherosclerosis Models. *JACC Cardiovasc. Imaging 9* (8), 950−961.
(27) Sanhai, W. R., Sakamoto, J. H., Canady, R., and Ferrari, M. (2008) Seven Challenges for Nanomedicine. *Nat. Nanotechnol. 3* (5), 242−244.
(28) Pérez-Medina, C., Abdel-Atti, D., Tang, J., Zhao, Y., Fayad, Z. A., Lewis, J. S., Mulder, W. J. M., and Reiner, T. (2016) Nanoreporter PET Predicts the Efficacy of Anti-Cancer Nanotherapy. *Nat. Commun. 7*, 7.
(29) Wright, B. D., and Lapi, S. E. (2013) Designing the Magic Bullet? The Advancement of Immuno-PET into Clinical Use. *J. Nucl. Med. 54* (8), 1171−1174.
(30) Badawi, R. D., Shi, H., Hu, P., Chen, S., Xu, T., Price, P. M., Ding, Y., Spencer, B. A., Nardo, L., Liu, W., et al. (2019) First Human Imaging Studies with the EXPLORER Total-Body PET Scanner. *J. Nucl. Med. 60* (3), 299−303.
(31) Mullard, A. (2013) Molecular Imaging as a De-Risking Tool: Coming into Focus? *Nat. Rev. Drug Discovery 12* (4), 251−252.
(32) Lee, H. B., and Blaufox, M. D. (1985) Blood Volume in the Rat. *J. Nucl. Med. 26* (1), 72−76.

DOI: 10.1021/acs.bioconjchem.9b00256
Bioconjugate Chem. 2020, 31, 360−368